Mitochondrial respiratory complex II is altered in renal carcinoma

BBA - Molecular Basis of Disease 1871 (2025) 167556

Contents lists available at ScienceDirect

BBA - Molecular Basis of Disease

journal homepage: www.elsevier.com/locate/bbadis

Mitochondrial respiratory complex II is altered in renal carcinoma

Sona Miklovicova [a,b], Luca Volpini [a,c], Ondrej Sanovec [a,b], Federica Monaco [c], Katerina Hadrava Vanova [d], Jaromir Novak [a,b], Stepana Boukalova [a], Renata Zobalova [a], Petr Klezl [e], Marco Tomasetti [c], Vladimir Bobek [e,f,g], Vojtech Fiala [h], Josef Vcelak [i], Lory Santarelli [c], Zuzana Bielcikova [h], Katerina Komrskova [a,b], Katarina Kolostova [e], Karel Pacak [d], Sarka Dvorakova [a,*], Jiri Neuzil [a,b,j,k,**]

[a] Institute of Biotechnology, Czech Academy of Sciences, 252 50 Prague-West, Czech Republic
[b] Faculty of Science, Charles University, 128 00 Prague, Czech Republic
[c] Department of Clinical and Molecular Sciences, Polytechnic University of Marche, 60126 Ancona, Italy
[d] Eunice Kennedy Shriver National Institute of Child Health and Human Development, National Institutes of Health, Bethesda, MD 20892, USA
[e] General University Hospital Kralovske Vinohrady, 100 34 Prague, Czech Republic
[f] Department of Thoracic Surgery, Krajska zdravotni a.s. and UJEP, 400 11 Usti and Labem, Czech Republic
[g] Department of Thoracic Surgery, Faculty of Medicine, Wroclaw University of Science and Technology, 51 377 Wroclaw, Poland
[h] General University Hospital, 128 08 Prague, Czech Republic
[i] Department of Molecular Endocrinology, Institute of Endocrinology, 110 00 Prague, Czech Republic
[j] School of Pharmacy and Medical Science, Griffith University, Southport, Qld 4222, Australia
[k] First Faculty of Medicine, Charles University, 121 08 Prague, Czech Republic

ARTICLE INFO

Keywords:
Complex II
Succinate dehydrogenase
Renal cell carcinoma
Metabolism
Mitochondria
Organoids

ABSTRACT

Background: Renal cell carcinoma (RCC) is a disease typified by anomalies in cell metabolism. The function of mitochondria, including subunits of mitochondrial respiratory complex II (CII), in particular SDHB, are often affected. Here we investigated the state and function of CII in RCC patients.
Methods: We evaluated tumour tissue as well as the adjacent healthy kidney tissue of 78 patients with RCC of different histotypes, focusing on their mitochondrial function. As clear cell RCC (ccRCC) is by far the most frequent histotype of RCC, we focused on these patients, which were grouped based on the pathological WHO/ISUP grading system to low- and high-grade patients, indicative of prognosis. We also evaluated mitochondrial function in organoids derived from tumour tissue of 7 patients.
Results: ccRCC tumours were characterized by mutated von Hippel-Lindau gene and high expression of carbonic anhydrase IX. We found low levels of mitochondrial DNA, protein and function, together with CII function in ccRCC tumour tissue, but not in other RCC types and non-tumour tissues. Mitochondrial content increased in high-grade tumours, while the function of CII remained low. Tumour organoids from ccRCC patients recapitulated molecular characteristics of RCC tissue.
Conclusions: Our findings suggest that the state of CII, epitomized by its assembly and SDHB levels, deteriorates with the progressive severity of ccRCC. These observations hold the potential for stratification of patients with worse prognosis and may guide the exploration of targeted therapeutic interventions.

1. Introduction

Renal cell carcinoma (RCC) is a hard-to-manage pathology. In spite of significant progress over the last decades in the diagnosis and treatment of RCC, patient outcome and prognosis remain poor [1,2]. This includes diverse histological subtypes such as clear cell, papillary, and chromophobe types of RCC. These subtypes vary in their cellular origins, with the clear cell (ccRCC) and papillary types arising from cells of the proximal convoluted tubule, while the chromophobe type originates from cells of the distal convoluted tubule within the nephron [3].

* Corresponding author.
** Correspondence to: J. Neuzil, Institute of BIotechnology, Czech Academy of Sciences, 252 50, Prague-West, Czech Republic.
E-mail addresses: sarka.dvorakova@ibt.cas.cz (S. Dvorakova), j.neuzil@griffith.edu.au, jiri.neuzil@ibt.cas.cz (J. Neuzil).

https://doi.org/10.1016/j.bbadis.2024.167556
Received 10 April 2024; Received in revised form 18 October 2024; Accepted 28 October 2024
Available online 31 October 2024

The most frequent ccRCC stands out among various malignancies due to its intricate metabolic reprogramming, primarily orchestrated by Von Hippel-Lindau (*VHL*) gene pathogenic variations [4] and the consequent modulation of hypoxia-inducible factors (HIFs), leading to upregulation of hypoxia-responsive genes [5]. These underlying alterations fuel tumour development, progression and metastasis, highlighting the urgency to dissect mitochondrial perturbations. From a clinical standpoint, ccRCC shows resistance to traditional cytotoxic drugs, with treatment strategies typically involving surgical interventions and targeted therapies like tyrosine kinase inhibitors, mTOR inhibitors, and immunotherapy [6]. Linked to this is the notion that high-grade (G3/4) patients exhibit markedly worse prognosis compared to low-grade (G1/2) patients [7]. Hence, it is of paramount importance to search for novel biomarkers and for improved targeted therapies.

Of particular interest in the case of ccRCC is the complex interplay between mitochondrial respiratory complex II (CII; succinate dehydrogenase, SDH) and the tumorigenic process. Although CII mutations are relatively rare in RCC [8], altered CII status has emerged as a notable negative prognostic marker in ccRCC [9], warranting a comprehensive investigation of RCC mitochondrial properties with focus on CII status and its assembly dynamics [10]. CII is at the crossroads of the Krebs cycle and oxidative phosphorylation (OXPHOS) as SDH, by means of its enzymatic activity, converts succinate to fumarate within the Krebs cycle, and the resulting electrons enter the electron transport chain (ETC), a step catalyzed by the succinate:quinone reductase (SQR) activity of CII [11]. CII is located at the inner mitochondrial membrane (IMM) and is composed of four nuclear-encoded subunits (SDHA, SDHB, SDHC, and SDHD). SDHA and SDHB are hydrophilic and are localized in the matrix, while SDHC and SDHD are hydrophobic and are buried in the IMM. Assembly of these subunits into CII is crucial for its function [10,11].

CII assembly is a complex process that involves maturation of its catalytic subunit SDHA as its crucial milestone, as we have recently reported [12]. We demonstrated that maturation of SDHA is step-wise, involving disordered-to-ordered alterations and sequential binding of assembly factors SDHAF2 and SDHAF4. Disruption of CII subunits or assembly factors leads to CII collapse or its aberrant assembly, resulting in metastable sub-assemblies referred to as CII_{low}, comprising SDHA alone or together with the assembly factors SDHAF2 and/or SDHAF4. Presence of CII_{low} indicates a stress situation [13].

We have recently conducted a Phase 1/1b clinical trial of MitoTam, an agent targeting mitochondrial complex I [14], where we found high benefit for ccRCC patients [15,16]. This is highly promising and indicates that MitoTam may be able to be developed into an efficient drug against RCC. It was recently proposed that anomalies in CII affect the level and assembly of CI, the target of MitoTam [17]. We therefore decided to systematically explore tumour tissue and the corresponding healthy kidney tissue for the state of CII.

2. Material and methods

2.1. Patients and tissue specimens

Tissue samples were obtained from patients undergoing total nephrectomy in 2 centers, i.e. University Hospital Kralovske Vinohrady (49 cases) and General University Hospital (29 cases), Prague, Czech Republic, between 2021 and 2024; and were inspected and reviewed by skilled pathologists. Tumours were graded according to the WHO/ISUP (World Health Organization/International Society of Urological Pathology) classification. Details of patients are presented in Table 1. Samples were transported to the laboratory on ice in the RPMI-1640 medium supplemented with 10 % fetal bovine serum (FBS) and 1 % penicillin/streptomycin (P/S) for immediate processing and stored at −80 °C till further analysis. In certain cases, the samples were analysed immediately, prior to freezing. Due to different requirements for fresh tissue and different amount of available patient material, individual assays were performed on different number of patient samples.

Table 1
Patient characteristics.

Parameter	Number of patients	%
(years) Age at diagnosis		
30–39	4	5
40–49	7	9
50–59	19	24
60–69	20	26
70–79	24	31
80–89	4	5
Gender		
Female	27	35
Male	51	65
Histology		
Clear cell	64	82
Papillary	8	10
Chromophobe	5	7
Oncocytoma	1	1
Grade		
Low (G1/2)	53	68
High (G3/4)	18	23
N/A	7	9
(cm) Tumour diameter		
1–2.9	10	13
3–5.9	34	44
6–8.9	18	23
9–12	8	10
N/A	8	10
TNM		
Benign	1	1
T1	33	45
T1N1	1	
T1M1	1	
T2	4	5
T3	33	49
T3N1	1	
T3M1	4	
Total	78	100

Ethics approval and consent to participate in the study was performed in accordance with the Declaration of Helsinki and was approved by the Ethical Review Committee of the Czech Health Research Agency, Reference number EK-VP/23/0/2022 and EK-VP/47/0/2020.

2.2. Primary cell culture

All chemicals were purchased from Sigma-Aldrich unless otherwise stated in the text. Tumour tissue samples were washed in cold PBS, minced and incubated for 1 h at 37 °C with DMEM/F12 medium (Lonza) supplemented with 1 % P/S, 5 mg/ml collagenase type II (Gibco) and 10 μM Y-27632. After enzymatic digestion, tissues were centrifuged at 200 *g* for 5 min at room temperature (RT). The supernatant was then discarded, and the pellet was incubated for 3 min at 37 °C with TrypLE Express Enzyme (Gibco). Trypsinization was neutralized with 20 % FBS and samples were centrifuged at 200 *g* for 5 min. The supernatant was then discarded and dissociated cell pellets were filtered through 100 μm cell strainers after resuspension in DMEM/F12 supplemented with 20 % FBS and 10 μM Y-27632. Dissociated and filtered cells were centrifuged at 200 *g* for 5 min, resuspended in organoid culture medium: DMEM/F12 supplemented with 10 % FBS, 1 % P/S, 10 ng/ml human epidermal growth factor (EGF), 5 μg/ml insulin and 0.4 μg/ml hydrocortisone; and seeded into T25 flasks. When confluent, primary cell cultures were

frozen at −80 °C in a solution of FBS with 10 % DMSO to establish patient-derived organoids.

2.3. Patient-derived organoid formation

Cell suspension corresponding to 70–80 % cell confluence was centrifuged at 200 *g* for 5 min at RT and resuspended in the same volume of ice-cold Matrigel (Corning). Drops of 20–25 μl of Matrigel-embedded cells were seeded into a 24-well plate and after solidification in the CO_2 incubator at 37 °C, 1 ml of the organoid culture medium was added to each well. Organoids were cultured for 2 weeks with medium changed every 3 days.

2.4. Histology and immunohistochemistry

After fixation in 4 % formaldehyde, organoids were embedded in 3 % agarose/PBS, followed by dehydration, paraffin embedding, sectioning, and standard hematoxylin and eosin (H&E) staining. Immunohistochemistry (IHC) staining was performed on paraffin sections (2 μm). Briefly, after deparaffinization and rehydration, sections underwent heat-mediated antigen retrieval. Endogenous peroxidase activity was neutralized by 20 min incubation with 3 % H_2O_2/methanol, followed by 1 h antigen blocking with 2 % bovine serum albumin (BSA). Sections were incubated with anti-carbonic anhydrase IX (CAIX) primary antibody (1:1000; Novus Biologicals, NB100–417). The primary antibody was diluted in the antibody diluent (Zytomed Systems) and incubated for 2 h at RT. Sections were subsequently incubated with ZytoChem Plus (HRP) One-Step Polymer anti-mouse/rabbit (Zytomed Systems) and visualized using a Liquid DAB+ substrate Chromogen System (Dako). Nuclei were counterstained with hematoxylin, and coverslips were mounted with the DPX (dibutylphthalate, polystyrene, xylene) reagent. Images were acquired using an optical microscope (DMi8 WF, Leica; 40× magnification).

2.5. Immunofluorescence

Immunofluorescence (IF) staining was performed on paraffin sections (2 μm). Briefly, after deparaffinization and rehydration, sections underwent heat-mediated antigen retrieval. After washing in PBS, sections were permeabilized with 0,05 % Tween20/PBS and incubated 1 h antigen blocking with 2 % bovine serum albumin (BSA). Subsequently, sections were incubated with anti-CAIX and anti-MT-CO1 primary antibodies (CAIX, 1:500, Novus Biologicals, NB100–417; MT-CO1, 1:100, Abcam, ab14705). The primary antibody was diluted in the antibody diluent (Zytomed Systems) and incubated for 2 h at RT. After additional washes in 0.05 % Tween20/PBS, sections were labelled with respective secondary antibodies (goat-anti-mouse AlexaFluorPlus 488, 1:300, Invitrogen, A32723 and goat-anti-rabbit AlexaFluorPlus 594, 1:300, Invitrogen, A32740). Final steps included further washes in 0.05 % Tween20/PBS and dH_2O followed by mounting with Vectashield containing DAPI (VECTASHIELD® Antifade Mounting Medium with DAPI Vector Laboratories H-1200-10). Sections were imaged using Nikon CSU-W1 confocal microscope, 20× CFI Plan Apo VC (NA = 0.75) objective and PRIME BSI camera (Teledyne Photometrics, 6.5 μm pixel size). using 405, 488 and 594 lasers complemented with corresponding emission filters (455/50, 525/50, 645/75). The unbiased quantification of mitochondria (MT-CO1) signal on healthy and tumour tissues was performed using FIJI software. To compare MT-CO1 level between healthy and tumour tissues, the nuclear (DAPI) signal was utilized to delineate tissue areas. This process involved denoising, background subtraction, and contrast enhancement, followed by automated local thresholding using the Bernsen method to create a mask. The same procedure was applied to compare MT-CO1 levels between tumour tissues and tumour organoids, with normalization to the CAIX membrane signal. The mean intensity of the MT-CO1 signal within the delineated tissue areas was measured using ImageJ.

2.6. CLARITY imaging

Organoids were processed using the CLARITY procedure [18]. Briefly, organoids were fixed in the CLARITY gel monomer containing 4 % formaldehyde for 2 h. After gel polymerization, organoids were cleared overnight in the clearing buffer (20 mM lithium hydroxide monohydrate and 200 mM SDS, pH 8,5) at 37 °C with gentle shaking. The next day, organoids were stained with DAPI and the lipophilic FM™ 4-64FX dye (Invitrogen). Stained organoids were mounted in the PROTOS refractive index matching solution. *Z*-stack images were acquired using the Carl Zeiss LSM 880 NLO confocal microscope (LD LCI Plan-Apochromat420852–9871, magnification 25×, N.A. 0.8). For 3D visualization and surface rendering, the Imaris software, v. 9.8.2 Package for Cell Biologists was used.

2.7. DNA and RNA isolation

Fresh-frozen tissues and cultured organoids were homogenized using 5 mm Stainless Steel Beads (Qiagen) and the Qiagen TissueLyser LT (Qiagen). DNA and RNA were extracted using the AllPrep DNA/RNA/Protein Mini Kit (Qiagen) for tissues and AllPrep DNA/RNA/Protein Micro Kit (Qiagen) for organoids according to the manufacturer's instructions. The concentration and purity of isolated DNA and RNA were assessed using a spectrophotometer (Nanodrop 2000 Instrument, Thermo Fisher Scientific), and the samples were stored at −80 °C until further analysis.

2.8. Genomic analysis of VHL gene using next generation sequencing

Genomic analysis was performed to characterize genetic alterations of the *VHL* gene using next-generation sequencing (NGS). Extracted DNA was amplified to generate 566 bp, 376 bp and 433 bp sequences of *VHL* exons 1, 2 and 3 using polymerase chain reaction (PCR) with primer pairs for exon 1: 5'-CGC GAA GAC TAC GGA GGT-3′ and 5′-GGA TGT GTC CTG CCT CAA G-3′, for exon 2: 5'-ACC GGT GTG GCT CTT TAA CA-3′ and 5'-GCC CAA AGT GCT TTT GAG AC-3′ and for exon 3: 5′-TGG CAA AGC CTC TTG TTC G-3′ and 5'-GCC CCT AAA CAT CAC AAT GCC-3′. 100 ng DNA was amplified with 1 μM of each primer and 1× Dream Taq PCR Master Mix (Thermo Fisher Scientific) in the final volume of 20 μl. 4 % DMSO was added to PCR reaction for exon 1. Cycling conditions were: denaturation step at 95 °C for 2 min followed by 35 cycles of denaturation at 95 °C for 20 s, annealing at 60 °C for 30 s (exons 2 and 3), or annealing at 53 °C for 30 s (exon 1), primer extension at 72 °C for 2 min and one final run-off extension at 72 °C for 10 min. All PCR products were visualized by electrophoresis using 2 % agarose gel in the TAE buffer. Libraries were prepared from purified PCR products of the *VHL* gene (exons 1, 2 and 3) using the Nextera XT DNA Library Prep Kit (Illumina) according to the manufacturer's sample preparation protocol and subsequently paired-end sequenced for 300 cycles by the MiSeq Reagent Kit v.2 on a MiSeq sequencer platform (Illumina). Sequence data were analysed by the on-instrument software Local Run Manager v.4 with DNA Amplicon Analysis Module v.2.1.0 (Illumina) with the option for somatic variant calling method from the Variant Caller. The data were demultiplexed and FASTQ files were generated. Reads from paired-end fragments were trimmed for low-quality and duplicate reads. The Local Run Manager software aligned the reads against the human reference sequence GRCH37.p5/hg19 using the Burrows-Wheeler Aligner (BWA) and Genome Analysis Toolkit (GATK, Broad Institute). All variants were visualized with the Integrative Genomics Viewer (UC San Diego, Broad Institute). The detected single-nucleotide variants and small insertions/deletions were annotated and filtered for exonic non-synonymous variants, variants with a probable splice site or frameshift effect and prediction of functional pathogenic effects in genetic databases ClinVar (http://www.ncbi.nlm.nih.gov/clinvar/) and VarSome (www.varsome.com).

2.9. Real-time PCR

1 μg RNA was reverse-transcribed into cDNA with random hexamer primers using Revert Aid First strand cDNA Synthesis Kit (Thermo Scientific). Target genes were amplified by real-time and fluorescent polymerase chain reaction using the 5xHOT FirePol Evagreen qPCR Supermix (Solis Biodyne) and the CFX96 Touch Real-Time PCR Detection System (BioRad). Relative mRNA levels were calculated as the fold change using the $2 - \Delta\Delta CT$ formula and were normalized to *GAPDH*. Primers were designed as follows: *SDHA* forward (5′- GAG ATG TGG TGT CTC GGT CCA T-3′), *SDHA* reverse (5′-GCT GTC TCT GAA ATG CCA GGC A-3′); *SDHB* forward (5′-CAG TCC ATA GAA GAG CGT GAG-3′), *SDHB* reverse (5′-TGT CTC CGT TCC ACC AGT AGC T-3′); *SDHAF2* forward (5′-CCA TAG AAA CCA AAA GAG CCC GC-3′), *SDHAF2* reverse (5′-AGG CGG TCA TAG AGG TTC AGC T-3′); *GAPDH* forward (5′- GTC GGA GTC AAC GGA TTT GG -3′), *GAPDH* reverse (5′- AAA AGC AGC CCT GGT GAC C-3′). The ratio of mitochondrial to nuclear DNA (mtDNA:nDNA) was analysed using primers for major arc of mtDNA: *MajArc* forward (5'-CTG TTC CCC AAC CTT TTC CT-3′), *MajArc* reverse (5'-CCA TGA TTG TGA GGG GTA GG-3′); and nuclear DNA primers for β2-microglobulin: *β2M* forward (5'-GCT GGG TAG CTC TAA ACA ATG TAT TCA-3′), *β2M* reverse (5'-CCA TGT ACT AAC AAA TGT CTA AAA TGG T-3′). Cycling conditions were: denaturation step at 95 °C for 2 min followed by 39 cycles of denaturation at 95 °C for 15 s, annealing at 60 °C for 20 s, and primer extension at 72 °C for 20 s.

2.10. High-resolution respirometry

6 mg of fresh healthy kidney and 14.5 mg of fresh tumour tissue were homogenized in the total volume of 2 ml of Mir05 medium (0.5 mM EGTA, 3 mM $MgCl_2$, 60 mM K-lactobionate, 20 mM taurine, 10 mM KH_2PO_4, 110 mM sucrose, 1 g/l essentially fatty acid-free BSA, and 20 mM HEPES, pH 7.1) using the PBI-Shredder O2k-Set (Oroboros), and transferred to the 2-ml chamber of the Oxygraph 2 k instrument (Oroboros). CII-mediated respiration was determined in the presence of 0.5 μM rotenone, 10 mM succinate, 3 mM ADP, and 10 μM cytochrome *c* at 37 °C. CII-specific oxygen-consumption rates were verified by the addition of 5 mM malonate. Antimycin A (2.5 μM) was added at the end of each assay to inhibit the electron transport chain, and residual oxygen consumption after antimycin A addition was subtracted from all results in order to obtain mitochondria-specific rates. Next, CIV activity was assessed after addition of 2 mM ascorbate and 0.5 mM tetramethyl-*p*-phenylenediamine (TMPD), followed by its inhibition with 1.25 mM potassium cyanide (KCN).

2.11. Citrate synthase activity

Citrate synthase (CS) activity was assessed spectrophotometrically using 10 μl tissue extracts after respirometry assays. Enzyme activity was determined by adding 0.31 mM acetyl-CoA, 0.5 mM oxalacetate and 0.1 mM 5,5′-dithiobis(2-nitrobenzoic acid) (DTNB). The absorbance at 412 nm was recorded for 30 min at 30 °C to measure the reaction product thionitrobenzoic acid (TNB) using a microplate reader (Infinite M200, Tecan). Regression analysis of the linear portion of the curve was performed using GraphPad PRISM software (v.8.4.3).

2.12. SDS-PAGE/western blotting

Tissues and organoids were homogenized in the Radio-ImmunoPrecipitation Assay (RIPA) buffer containing 20 mM Tris (pH 7.5), 150 mM NaCl, 1 mM EDTA, 1 mM EGTA, 1 % (*v*/v) NP-40, 0.1 % SDS and 0.5 % sodium deoxycholate supplemented with the protease inhibitor mix M (Serva) buffer using 5 mm Stainless Steel Beads (Qiagen) and TissueLyser LT (Qiagen). The solution was shaken for 1 h on ice. Lysed tissue was centrifuged at 16,000 *g* for 5 min at 4 °C, and the supernatant was collected for analysis. Total protein was quantified by the Pierce BCA Protein Assay Kit (Thermo Scientific). Following boiling in the 4× Laemmli sample loading buffer (8 % SDS, 260 mM Tris-HCl, pH 6.8, 40 % glycerol, 200 mM DTT, 0.01 % bromophenol blue) for 5 min, 40 μg of the denatured protein was loaded and separated using 12 % SDS-PAGE gel. Wet blotting was used to transfer the separated proteins to 0.45 μm pore nitrocellulose membrane (BioRad). The membrane was blocked with 5 % non-fat milk for 1 h and incubated overnight at 4 °C with the diluted solutions (1:1,000) of primary antibodies in Tris-buffered saline/Tween-20 (TBS-T) supplemented with 2 % non-fat milk. The following primary antibodies were used: anti-Hsp60 (12,165, Cell Signaling), anti-β-actin (8457S, Cell Signaling), anti-SDHA (ab14715, Abcam), anti-SDHB (ab14714, Abcam), anti-SDHAF2 (45,849, Cell Signaling), anti-CAIX (NB100–417, Novus), anti-Tomm20 (sc11415, Santa Cruz). Horseradish peroxidase-conjugated secondary antibodies were used in TBS-T with 2 % non-fat dried milk for 1 h at RT (1:5000 for goat anti-mouse IgG (170–6516, BioRad); and goat anti-rabbit IgG (170–6515, Biorad)). Protein bands were detected by the chemiluminescent HRP substrate (Radiance ECL or Radiance Plus, Azure Biosystems) using the Azure 600 Instrument and AzureSpot 2.0 Software (Azure Biosystems). The intensity of each band was evaluated by ImageJ software (ImageJ, v.1.8.0), and was normalized according to the β-actin level.

2.13. Isolation of mitochondria

To isolate mitochondria, healthy kidney and tumour tissues were homogenized on ice in the isolation buffer (225 mM mannitol, 75 mM sucrose, 5 mM HEPES-KOH, pH 7.4, 1 mM EGTA) with 1 % BSA using chilled Dounce Tissue Grinder (Kimble Chase, DWK Life Sciences). The homogenate was centrifuged at 1000 *g* for 10 min at 4 °C. The supernatant containing mitochondria was collected and then centrifuged at 10,000 *g* for 10 min to pellet mitochondria. Pelleted mitochondria were washed with the isolation buffer and stored at −80 °C.

2.14. Native blue gel electrophoresis/western blotting

10 μg digitonin-solubilized (8 g/g protein) mitochondria were mixed with the sample loading buffer (0.015 μl per 1 μg protein; 0.75 M aminocaproic acid, 50 mM Bis-Tris, 12 % glycerol, 0.5 mM EDTA, 5 % Coomassie Brilliant Blue G-250) and separated on a 4–16 % NativePAGE Novex BisTris gradient gel (Life Technologies). Electrophoresis ran in three steps, i.e., using the blue cathode buffer (0.02 % Coomassie Brilliant Blue G-250) at 35 V for 70 min, and then clear cathode buffer at 25 V overnight. Finally, the voltage was increased to 200 V for 2 h. For western blotting, gels were incubated in the transfer buffer for 10 min with 0.1 % SDS, and proteins were transferred to 0.2 μm polyvinylidene difluoride (PVDF) membrane (BioRad). Western blot analysis following native gel electrophoresis was conducted using the same procedure as for SDS-PAGE (see above).

2.15. In-gel succinate dehydrogenase (SDH) activity

To assess in-gel SDH activity, 30 μg digitonin-solubilized mitochondria were mixed with 10× sample buffer containing 50 % glycerol and 0.1 % Ponceau S dye, then subjected to high-resolution clear native electrophoresis. Cathode buffer was supplemented with 0.05 % deoxycholate and 0.01 % lauryl maltoside. Electrophoresis was performed on a 4–16 % NativePAGE Novex Bis-Tris gel at 35 V for 70 min, followed by overnight running at 25 V and an additional 2 h at 200 V. To visualize the activity, gels with separated protein complexes were incubated for 20 min in an assay buffer containing 20 mM sodium succinate, 0.2 mM phenazine methosulfate, and 0.25 % nitrotetrazolium blue in 5 mM Tris-HCl (pH 7.4). The reaction was stopped using a solution of 50 % methanol and 10 % acetic acid, and gels were immediately photographed.

2.16. Succinate:quinone reductase activity

Tissue was lysed in 25 mM phosphate potassium buffer (pH 7.4) using the PBI-Shredder O2k. Protein lysates (12.5 µg) were resuspended in 100 mM phosphate buffer and transferred to a 96-well plate. The lysates were then incubated in a buffer containing 20 mM succinate, 2 µM antimycin A, 5 µM rotenone, 10 mM sodium cyanide, 50 mg/ml bovine serum albumin, and 0.015 % *w/v* 2,6-dichlorophenol indophenol for 5 min. The signal intensity at 600 nm was recorded for 5 min, after which 100 µM decylubiquinone was added and the reaction was recorded for 30 min. Identical measurements were performed in the presence of 20 mM malonate, and net SQR activity was obtained by subtracting the malonate-insensitive rate. Regression analysis of the linear portion of the curve was performed using GraphPad PRISM software (v.8.4.3).

2.17. Statistical analysis

The data are presented as mean values ± standard error of mean (SEM). Non-parametric tests were used due to the non-normal distribution of most parameters, evaluated using Shapiro-Wilk normality test. Group differences were evaluated using Wilcoxon and Mann-Whitney test using GraphPad Prism (v.8.4.3). Significant differences were considered at $p < 0.05$.

3. Results

3.1. Clinical, pathological and molecular characteristics of RCC patients

Table 1 shows the overview of characteristics of 78 patients whose biological material, i.e. RCC tissue and adjacent healthy kidney tissue,

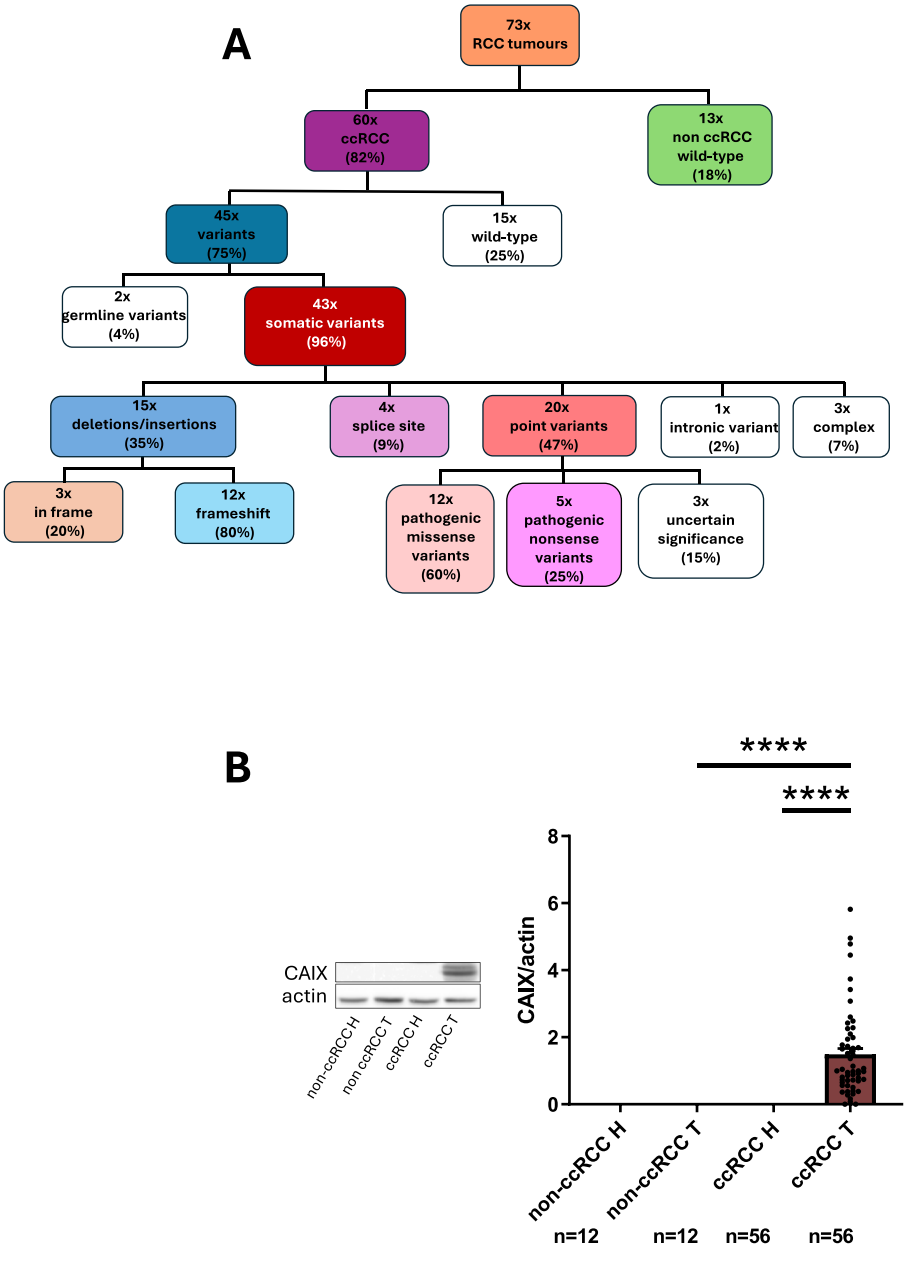

Fig. 1. ccRCC is characterized by von Hippel-Lindau gene variants and expression of carbonic anhydrase IX.
ccRCC and non-ccRCC tumour and healthy kidney tissue were evaluated for the presence of *VHL* gene variants (A). The tissue was evaluated by WB for the CAIX protein (B); lower panel, evaluation of CAIX using densitometry; upper panel, representative WB. Data are mean values ± SEM. Sample sizes are indicated within group labels. Statistical significance is indicated by asterisks, with the symbol of **** indicating $p < 0.0001$.

was used in this study. The age and gender are shown, with about 2 times more males than females. >80 % of patients had ccRCC, with the rest diagnosed with papillary or chromophobe RCC and renal oncocytoma. Concerning the grade, 68 % cases were classified as low-grade (G1/2), 23 % as high-grade (G3/4); 9 % of patients were not classified. Regarding tumour size, the majority of patients had tumours with diameters ranging from 3 to 6 cm.

Patients were classified according to the TNM staging, which includes three independent components: T (tumour size and extent), T1 includes tumours ≤7 cm in diameter confined to the kidney, T2 tumours >7 cm confined to the kidney, T3 tumours extending beyond the kidney but still within Gerota's fascia; N (lymph node involvement, N0/1), and M (distant metastasis, M0/1). Most patients had T1 and T3 tumours and only 5 patients presented with distant metastases.

Sporadic ccRCC is typified by frequent somatic *VHL* pathogenic variants. To assess this in our patient cohort, we sequenced 3 exons of the *VHL* gene from the tumour and healthy tissue of patients for the detection of variants in the gene. Fig. 1A shows that ~75 % of ccRCC tumours had *VHL* variants, while papillary or chromophobe RCC and renal oncocytoma tissue exhibited only wild-type *VHL*. We next investigated what types of pathogenic variants are present in ccRCC and found unique somatic variants in nearly all the patients including point variants, deletions/insertions and splice site variants (Fig. 1A). A detailed list of *VHL* pathogenic variants in our patient cohort, ordered by the position in the gene, is presented in Table S1. Additionally, we investigated carbonic anhydrase IX (CAIX) as a potential marker for kidney tumours at protein level. Western blot analysis revealed that CAIX is a reliable marker of ccRCC as it is not expressed in non-ccRCC tumours (Fig. 1B).

3.2. Clear cell renal carcinoma exhibits low mitochondrial content and CII status

As ccRCC is by far the most prevalent type of RCC, our primary focus was on patients with this tumour subtype. We first evaluated the level of mitochondria in different types of RCC as well as in the corresponding healthy kidney tissue, pooling data of non-ccRCC tumours together. Fig. 2 shows evaluation of the CIV capacity (A), mitochondrial enzyme CS activity (B), mtDNA level (C), amount of mitochondrial protein (D) and the level of the mitochondrial marker Hsp60 (E), all of which were significantly lower in tumour tissue compared to healthy kidney tissue of ccRCC patients and compared to pathological and healthy kidney tissue of non-ccRCC patients. Importantly, while there were differences between tumour tissue from ccRCC and non-ccRCC patients in all evaluated parameters, those of healthy kidney tissue from ccRCC and non-ccRCC patients were highly similar. These data indicate that tumours of non-ccRCC histotypes preserve the CIV capacity, CS enzyme activity and ETC function. Interestingly, the mtDNA/nDNA ratio (C) in non-ccRCC tumours was greater than that in corresponding healthy kidney, suggesting greater mitochondrial ETC contribution to metabolism in these tumour histotypes. Notably, we also observed low MT-CO1 IF staining in clear cell tumour tissues compared to adjacent healthy kidney tissue (Fig. 2F).

We next assessed the level and activity of CII in the same patient cohorts. Fig. 3 shows CII-dependent respiration (A), SQR activity (B), *SDHA* (C) and *SDHB* (D) transcripts, and the level of the SDHA and SDHB protein as well as the level of the SDHAF2 protein (since this assembly factor is associated with CII assembly status) (E). Similarly to the level of mitochondrial protein, we also found significantly decreased CII and in CII-related activities between ccRCC tumour tissue and non-ccRCC tumour tissue. Again, the two types of healthy kidney tissue were similar to each other (Fig. 3).

Finally, we tested the premise that mitochondrial status and CII respiration may differ in patients according to gender and age. Given the significant differences in mitochondrial parameters observed between clear cell and other histotypes and considering that clear cell is the most common histotype in both clinical practice and our cohort, combining them would introduce bias. Therefore, we focused this analysis exclusively on clear cell patients. Fig. S1 illustrates that there were no significant differences between genders, nor age groups (32–60 vs. 61–87 years of age at diagnosis) in terms of CII-dependent respiration (A), SQR activity (B), CIV capacity (C), CS activity (D) and mtDNA level (E).

3.3. Mitochondrial content increases with the grade of ccRCC

In the next analyses, we focused on tumour and healthy tissue from ccRCC patients according to the tumour grade using a simplified 2-tiered grading system, combining low G1/2 and high G3/4, as recommended by contemporary pathology practice [19,20]. This approach has been shown to be as effective as the traditional 4-tiered grading system in predicting cancer-specific mortality [21].

Since mitochondrial characteristics, including CIV capacity, CS activity and the level of mitochondrial proteins differed only marginally (not reaching significance) in healthy kidney tissue from G1/2 and G3/4 ccRCC patients (Fig. S2), we expressed these mitochondrial features in the corresponding tumour tissues relative to those in healthy kidney tissue. Interestingly, Fig. 4 shows that the level of mitochondria, based on the evaluated features of CIV capacity (A), CS activity (B) and isolated mitochondrial protein (C), increased with tumour grade. This indicates that with increasing grade of RCC, tumour tissue is characterized by increased mitochondrial status/function.

3.4. Increasing grade of ccRCC is accompanied by altered CII status

Having characterized ccRCC samples for their mitochondrial status, we decided to evaluate them also for properties of CII, relating these various analyses to corresponding healthy kidney tissue. Fig. 4 shows CII-dependent respiration (D), SQR activity (E) and SDH activity (F), related to the loading control. While there were no differences in CII-dependent respiration (D) and SQR activity (E) between G1/2 and G3/4 tissue, SDH activity (F) in isolated mitochondria was significantly decreased in G3/4 patients. We then evaluated the CII subunits SDHA and SDHB and the assembly factor SDHAF2, at the transcript (G, H, I) and protein (J, K, L, M) level, and found no significant differences (Fig. 4).

Interestingly, the pattern was quite different when we assessed CII assembly using NBGE/WB in isolated mitochondria. Fig. 4N shows that the proportion of CII_{low} sub-assemblies within total CII was higher in G3/4 ccRCC patients compared to their G1/2 counterparts and compared with healthy tissue from G3/4 patients, with the statistics shown in Fig. 4O-P. This is supported by lower level of SDHB in assembled CII compared to SDHA (Fig. 4Q), and higher level of SDHAF2 (Fig. 4R), again comparing G3/4 and G1/2 patients. Since SDHA appears to be stable within individual tissues, we used the level of this subunit as the loading control. These results show that while the function of CII in terms of CII-dependent respiration or the level of CII subunits does not change with the patient grade, the more aggressive ccRCC tumours appear to have lower level of fully assembled CII, higher level of CII sub-assemblies and lower SDH activity per mitochondrial amount.

3.5. Tumour organoids resemble the expression pattern of mitochondrial proteins of parental tissue

A recent approach used to recapitulate tumours in tissue culture is based on the use of organoids. We therefore prepared organoids from tumour tissue and assessed their mitochondria-linked properties, as we did for the patient tissue, with the idea that they may recapitulate properties of tissue samples shown above. To achieve this, we prepared organoids from 7 patients (patients 61, 62, 64, 68, 70, 73, 76). Fig. 5A documents successful formation of organoids from tumour tissue, clearly revealing the 3D and 2D structure of the same tissue, and indicating the presence of cell mass in tumour tissue organoids.

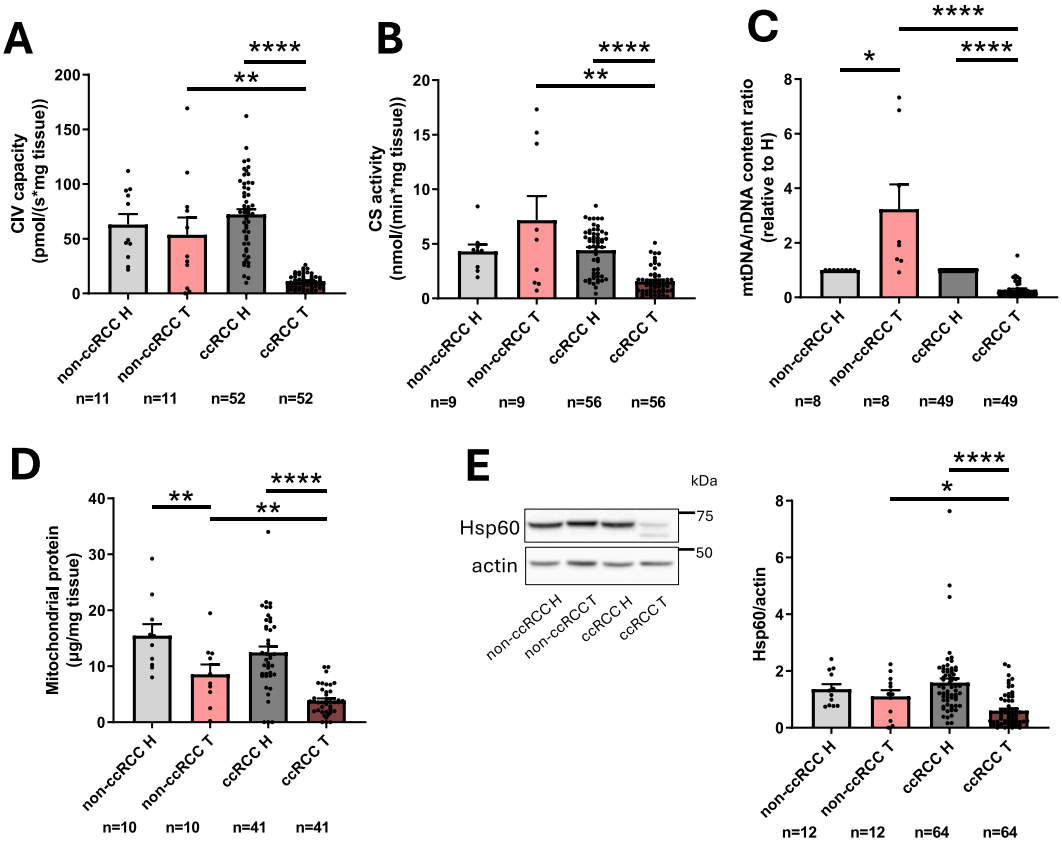

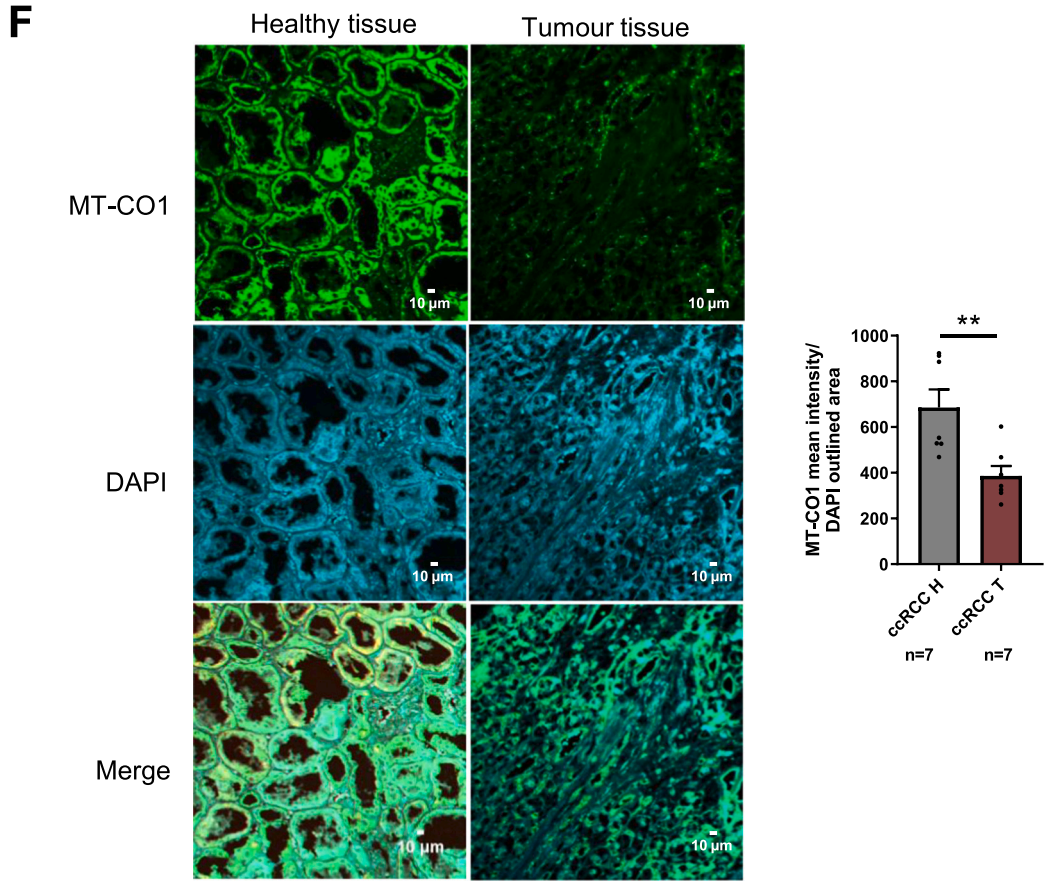

(caption on next page)

Fig. 2. ccRCC tumour tissue shows low mitochondrial expression, protein levels and function.
ccRCC and non-ccRCC tumour and healthy kidney tissue was evaluated for CIV capacity (A), CS activity (B), mtDNA/nDNA ratio (C), amount of mitochondrial protein (D), and the level of the mitochondrial marker Hsp60 (E). Panel E shows representative western blot (left), and densitometric evaluation of the level of the Hsp60 protein in patients (right). (F) Representative immunofluorescence images from paraffin-embedded sections of healthy and tumour tissue (Scale bar = 10 μm). MT-CO1 expression was analysed using ImageJ for unbiased quantification. Mean MT-CO1 intensity measured on DAPI outlined was compared between healthy and tumour tissues. The MT-CO1-stained image of tumour tissue (upper right panel) represents the same image as shown in Fig. 5I (middle left panel). Data are mean values ± SEM. Sample sizes are indicated within group labels. Statistical significance is indicated by asterisks, with the symbol of * indicating $p < 0.05$, symbol of ** $p < 0.01$, symbol of *** $p < 0.001$, symbol of **** $p < 0.0001$.

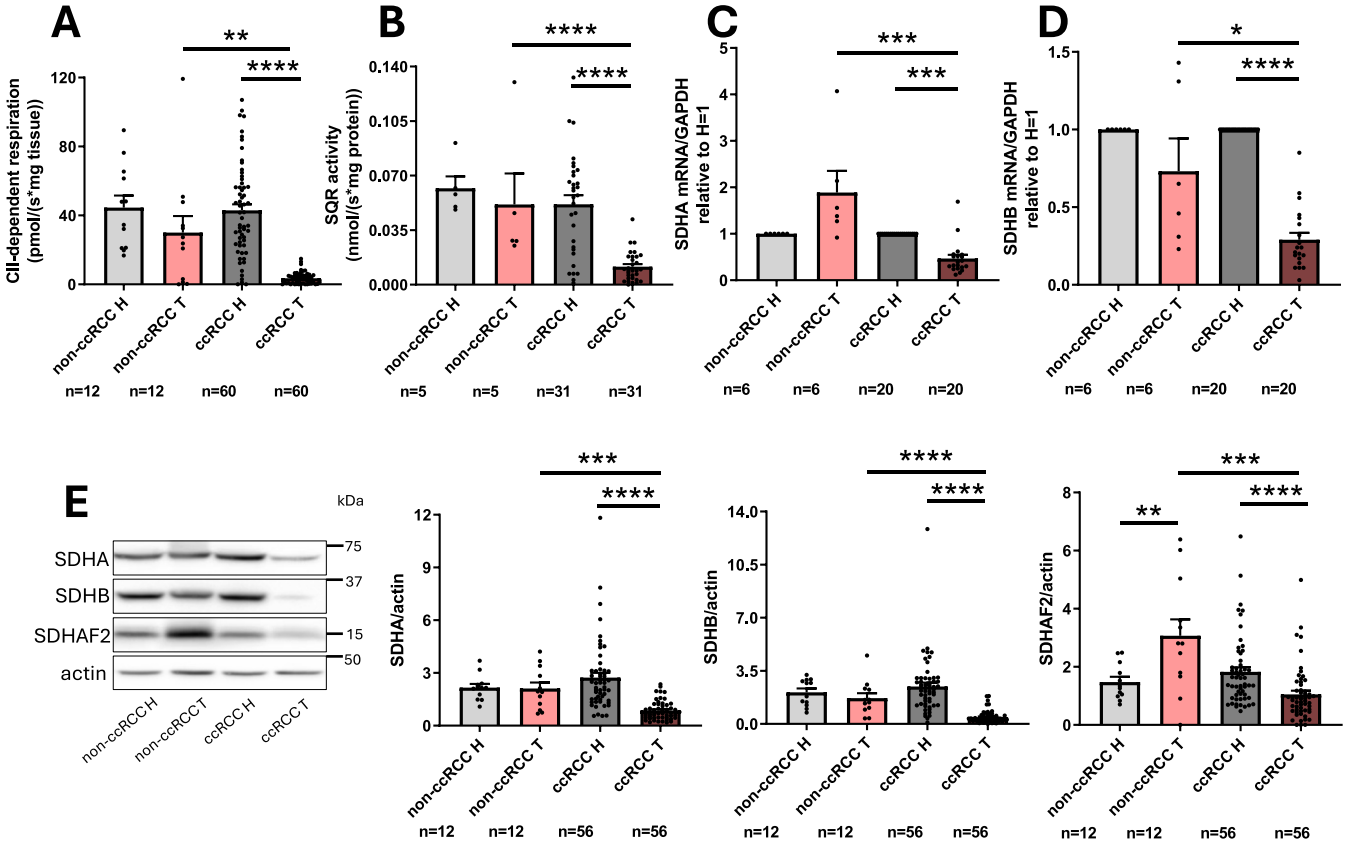

Fig. 3. Complex II function is lower in ccRCC than in other RCC types and non-tumour tissue.
ccRCC and non-ccRCC tumour and corresponding healthy kidney tissue was evaluated for CII-dependent respiration (A), SQR activity (B), *SDHA* mRNA (C), *SDHB* mRNA (D), and the level of the CII subunits SDHA and SDHB and the CII assembly factor SDHAF2 (E). Panel E shows a representative western blot (left) and densitometric evaluation (right). Data are mean values ± SEM. Sample sizes are indicated within group labels. Statistical significance is indicated by asterisks, with the symbol of * indicating $p < 0.05$, symbol of ** $p < 0.001$, symbol of **** $p < 0.0001$.

We found identical somatic *VHL* pathogenic variants in organoids and tumour tissues of the same patient (Table S1). This result underscores the reliability of the organoid model in recapitulating the *VHL* status of the original tumour. We then characterized organoids for their morphology using H&E staining and also assessed the state of CAIX, with a representative image in Fig. 5B and images for other matching tissues and organoids in Fig. S3. Of note, the CAIX staining pattern of parental tissues (low/no in healthy vs. high in tumour) is consistent with the results obtained from SDS-PAGE and western blotting of healthy and tumour tissue (Fig. 1B). By combining these two methods, we ensure both quantitative accuracy and spatial context, providing more robust and comprehensive characterization. Finally, we evaluated organoids for the level of mitochondrial proteins, including SDHA, SDHB and SDHAF2, and compared them with their levels in the corresponding tissue (Fig. 5C). We found no significant differences in the levels of Hsp60, Tomm20, SDHA, SDHB and SDHAF2 between tumour tissue and tumour organoids (Fig. 5D-H). We also performed MT-CO1 immunofluorescence staining, which revealed that the complex IV subunit, indicative of mitochondrial content, is comparable to levels observed in tumour tissue (Fig. 5I).

Collectively, these data indicate that organoids derived from kidney tumour tissue recapitulate the mitochondrial status of corresponding patient tumour tissue.

4. Discussion

In this research, we analysed healthy and tumour tissue from ccRCC and non-ccRCC patients for their mitochondrial status and the status and function of mitochondrial respiratory CII. Our study was motivated by the need to advance our understanding of mitochondrial involvement in RCC and its implications for therapeutic strategies. We were also encouraged to undertake this investigation based on our recent MitoTam clinical trial, where this mitochondrially targeted anti-cancer drug acts by disrupting mitochondrial respiratory complex I [14]. More specifically, the Phase1/1b clinical trial, which enrolled 75 patients with various diagnoses, revealed that those with RCC experienced the highest efficacy of the therapy, where 5 out of 6 RCC patients showed benefit from the treatment (either long-term stabilization or remission) [16]. All

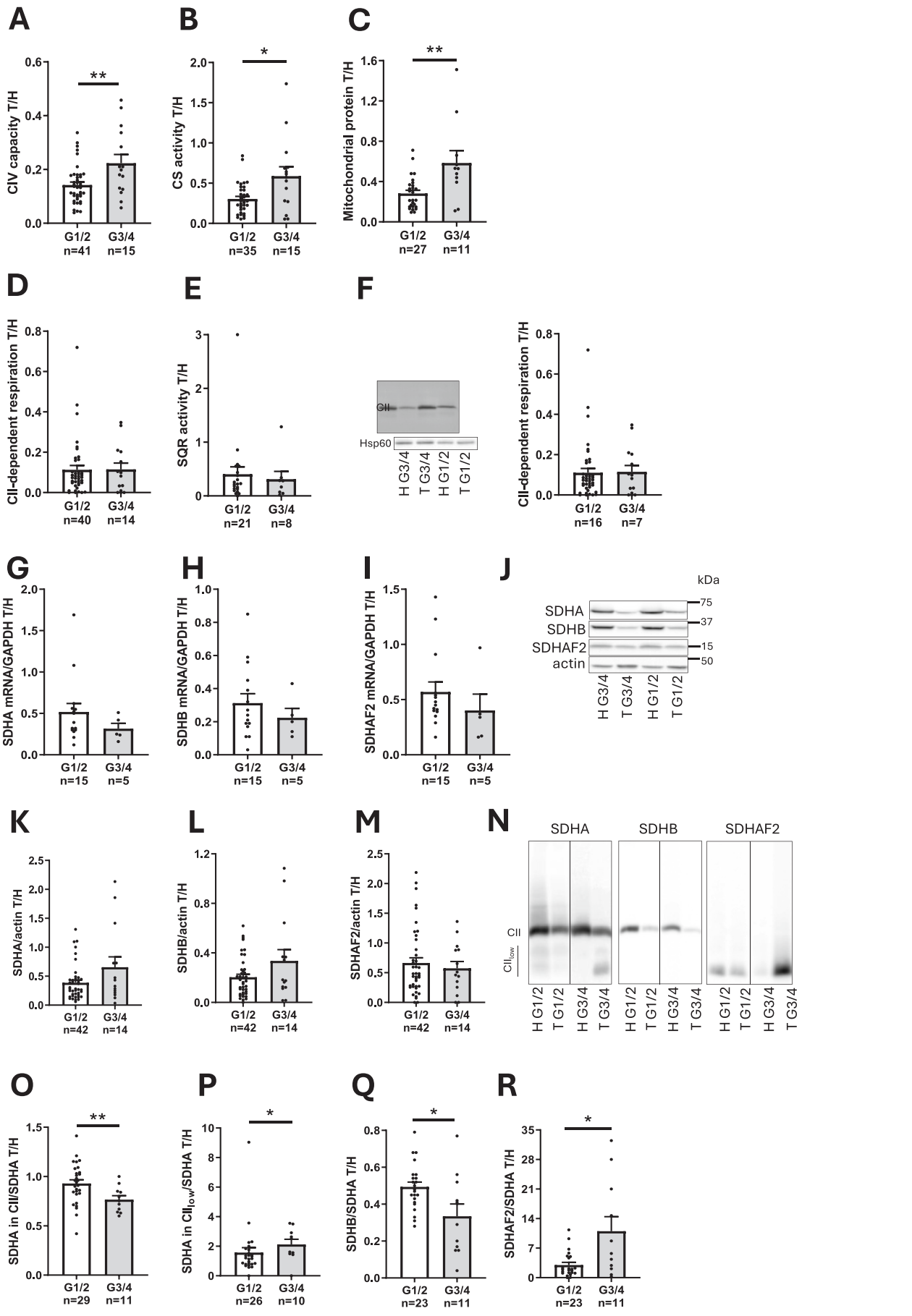

(caption on next page)

Fig. 4. Mitochondrial content, but not CII increases with tumour grade in ccRCC.
Tumour tissue from patients with Grade 1/2 and patients with Grade 3/4 was evaluated for CIV capacity (A), CS activity (B), amount of mitochondrial protein (C), CII-dependent respiration (D), SQR activity (E) and in-gel SDH activity (F), relative to healthy kidney tissue. Data in panel F are related to the loading control Hsp60. Grade 1/2 and Grade 3/4 patient tumour tissues were further evaluated for the expression of *SDHA*, *SDHB* and *SDHAF2* mRNA (G-I) and for the level of SDHA, SDHB and SDHAF2 protein using SDS-PAGE/WB (J, representative image; K-M, densitometric evaluation). Panel N shows a representative image of NBGE/WB for SDHA, SDHB and SDHAF2 in tumour and healthy tissue, and the level of SDHA in CII (O), amount of SDHA in CII_{low} (P), and the ratio of SDHB/SDHA (Q) and SDHAF2/SDHA (R). Data shown are mean values ± SEM. Sample sizes are indicated within group labels. Values of tumour tissue are related to corresponding healthy kidney tissue values. Statistical significance is indicated by asterisk, with the symbol of * indicating $p < 0.05$, symbol of ** indicating $p < 0.01$.

five patients with benefit were diagnosed with ccRCC [15]. With relevance to the effect of MitoTam on ccRCC patients via CI destabilization, it has been suggested that anomalies in CII affect CI, as shown for example in cells derived from an RCC patient with a nonsense pathogenic variant in the *SDHB* gene [17,22], or in HEK-293 SDHA KO cells [23]. Finally, RCC is known to frequently harbour anomalies in subunits and assembly factors of CII [9]. We therefore evaluated the mitochondrial status of RCC patients with a focus on CII.

VHL mutations are common in ccRCC, and we identified *VHL* variants in 75 % of our cohort of ccRCC patients, consistent with previous studies [24,25]. Our results support previous reports indicating that somatic *VHL* pathogenic variants are specific for this histotype, as we did not find *VHL* variants in other tumours [26]. Recent evidence supports the significance of *VHL*-deficient cells, suggesting that neither wild-type *VHL* nor *VHL* knockout (KO) cells alone can initiate metastasis. Instead, metastatic colonization occurs only when both cell populations co-exist, driven by secretion of pro-metastatic factors by *VHL* KO cells [27]. We identified three patients with shared splice site *VHL* pathogenic variants. Interestingly, all other sequenced tumours exhibited unique *VHL* variants (except Gln73Ter) across all three exons, without any shared variants among patients, indicating a lack of discernible hotspots. This observation aligns with findings suggesting the absence of hotspots and genotype-phenotype correlations in *VHL* pathogenic variants [28], despite ongoing efforts to predict *VHL* functional consequences using in silico methods [29]. This further emphasizes the unique properties of ccRCC.

Our results demonstrate a reduction in mitochondrial content and activity within ccRCC tumours, as evidenced by suppressed TCA cycle activity assessed by CS activity, and compromised OXPHOS function indicated by lower CIV capacity. We hypothesized that these changes in mitochondrial function could stem from a reduction in mtDNA content, and we found decreased mtDNA/nDNA ratio, which could be linked to lower expression of mtDNA-encoded genes. Indeed, low mtDNA content has been shown to downregulate ETC complex subunits, implying a direct link between mtDNA depletion and reduction in ETC proteins [30]. Therefore, a decrease in mtDNA may cause reduced OXPHOS in ccRCC.

In ccRCC, reduced mitochondrial transcription factor A (TFAM) expression results in decreased level of this mtDNA-binding protein, leading to impaired mtDNA transcription and replication [53]. Consequently, reduced TFAM-mediated regulation of mtDNA can contribute to the observed decrease in mtDNA content in ccRCC tumours. Linked to this, TFAM was previously found to be attenuated in ccRCC due to decreased level of the co-activator protein PGC1α [31]. Moreover, wild-type VHL is implicated in protecting TFAM from degradation by the LONP protease in kidney tissue, however in case of mutated *VHL*, TFAM is no longer protected from the degradation, which has negative impact on mitochondrial biogenesis in ccRCC tumour tissue [32]. This may imply that overall mitochondrial metabolism is suppressed in ccRCC tumours compared to adjacent healthy kidney tissue, explaining differences between ccRCC and other RCC histotypes. This suggests that ccRCC tumours differ from other types of RCC, which may impact their therapeutic options.

Despite impairment in mitochondrial function, ccRCC cells can sustain their energy metabolism and biosynthetic processes via glycolysis and other compensatory metabolic mechanisms, facilitating tumour growth and progression [33]. In contrast, the metabolic landscape of chromophobe or papillary RCC, due to their low frequency, remains relatively unexplored. Our study contributes to this gap by demonstrating preserved mitochondrial and CII content in chromophobe and papillary RCC. These findings contrast with an earlier report pointing to decreased ETC activity in papillary and chromophobe RCC [30], underscoring the need for further investigation of the metabolic heterogeneity in various RCC histotypes.

We observed aberrant function of CII in ccRCC tissue, manifested as reduced CII-dependent respiration. Moreover, SQR activity, critical for channeling electrons from the conversion of succinate to fumarate, catalyzed by SDH, to the ETC, was notably decreased compared to other histotypes and adjacent healthy kidney tissue. The underlying mechanism of CII inhibition in ccRCC tumours could be linked to high expression of NDUFA4L2, as this protein was previously shown to inhibit OXPHOS by targeting CI- and CII-dependent respiration in skeletal muscle and, importantly, in ccRCC [34,35]. Consequently, NDUFA4L2 may serve as a potential marker of ccRCC. Our findings collectively support the emerging understanding of ccRCC as a distinct RCC type characterized by dysregulated mitochondrial function, including CII properties.

Having observed suppression of mitochondrial metabolism in ccRCC, we decided to delve deeper into its implications for disease progression. Histological grade of tumours serves as a prognostic factor of cancer progression, with higher grade tumours often associated with increased metastatic potential. With this in mind, we compared metabolic changes of high- and low-grade tumours. We found that mitochondrial content and activity increased with grade, which is consistent with a recent study indicating re-activation of OXPHOS in metastatic tumours [36]. Interestingly, a negative correlation was found between OXPHOS levels and survival in metastatic patients [37], while another study indicated higher mtDNA content and CS activity in high-grade compared to low-grade tumours [38]. It is now considered a common characteristic that advanced stage RCCs require extensive transformation of their genomic landscape [39]. There is evidence indicating that the loss of the *SETD2* gene (coding for histone methyltransferase) is essential alongside *VHL* for tumour progression, leading to metastasis, invasion, presence of rhabdoid features, and necrosis [40]. Indeed, *SETD2* loss led to increased OXPHOS through the upregulation of PGC1α expression [41].

Surprisingly, we found no significant differences in the levels of CII subunits SDHA and SDHB, and the assembly factor SDHAF2 by SDS-PAGE/WB, or CII-dependent respiration and SQR activity between high-grade and low-grade tumours. These findings align with recent research identifying CII dysfunction as a negative prognostic indicator, with a distinct category of SDH-deficient tumours bearing mutations in CII [42–45]. Low CII activity in ccRCC is particularly noteworthy given that CII subunits, unlike those of other ETC complexes, are exclusively encoded by nuclear DNA, while mechanisms underlying the observed low level of CII function in ccRCC remain elusive. Prior studies have suggested a potential involvement of promoter methylation [46,47], direct inhibition of *SDHD* by miRNAs, and deletions of *SDHB* [9]. Intriguingly, more detailed analysis using NBGE/WB linked to CII assembly, crucial for its function, revealed decreased SDHB level and lower level of fully assembled CII in high-grade tumours, accompanied by increased levels of SDHA and SDHAF2 within the CII sub-assembly termed CII_{low}. We also found lower SDH activity in high-grade tumours. These findings suggest lower efficacy in CII assembly, possibly due to reduced SDHB availability and accumulation of CII_{low}, where

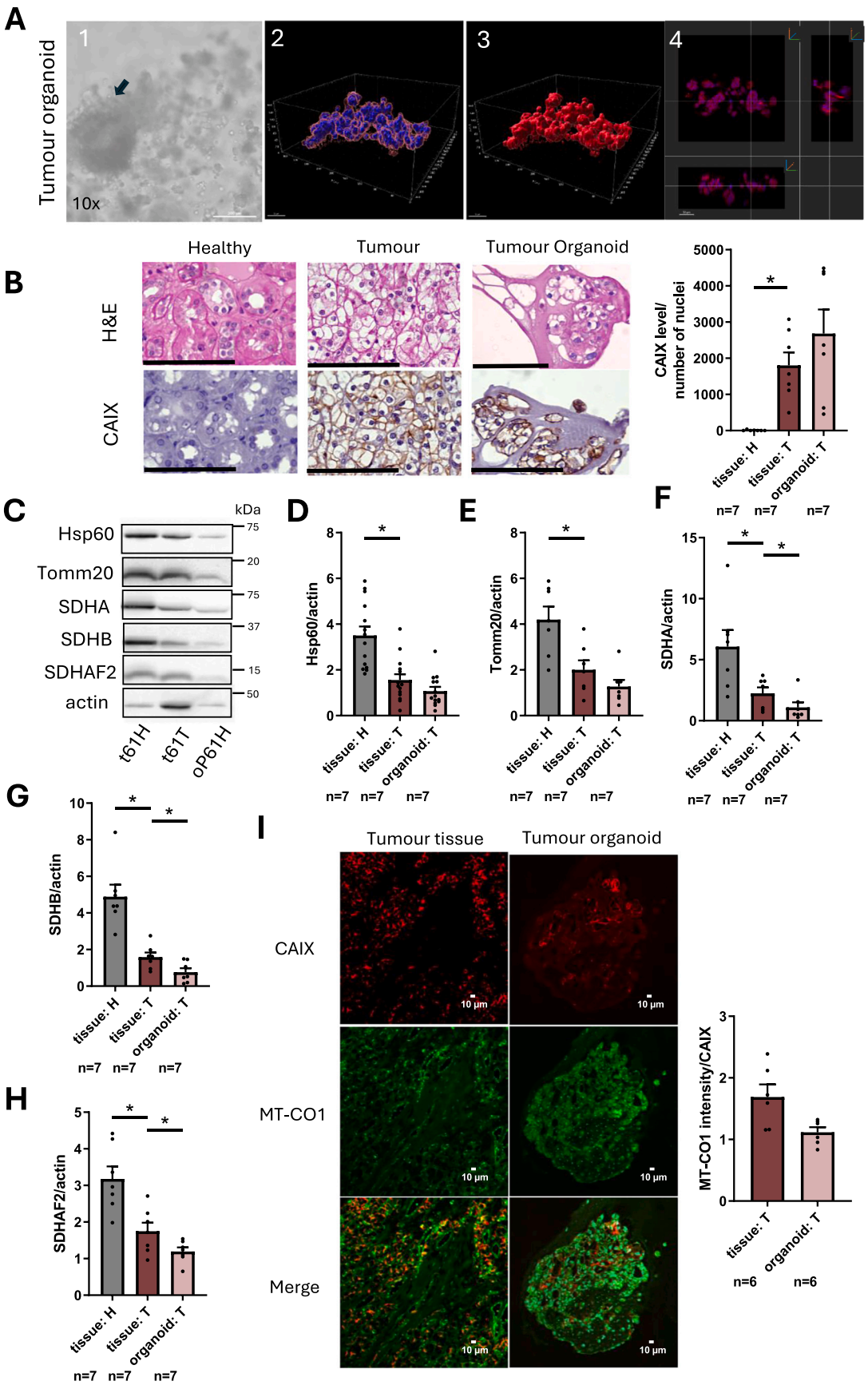

(caption on next page)

Fig. 5. Organoids from ccRCC patients recapitulate ccRCC tissue.
Phenotypic comparison of 3D organoids with parental tumour characteristics. (A1) Brightfield images (scale bar = 200 μM) of organoids derived from tumour tissue.; (A2) 3D visualization of surface-rendered nuclei and membranes in optically cleared organoids with Imaris software. Nuclei (blue); membranes (red) (A3) 3D surface rendering of membranes. (A4) orthogonal projections (scale bar = 50 μm). (B) H&E staining and CAIX staining of organoids and corresponding parental tissue from patient 76. The same H&E and CAIX images for this patient are also shown in Fig. S3. (C) WB showing levels of (D) Hsp60, (E) Tomm20, (F) SDHA, (G) SDHB, (H) SDHAF2 per the loading control actin. (I) Representative immunofluorescence images from paraffin-embedded sections of tumour tissue and tumour organoids (Scale bar = 10 μm). MT-CO1 expression was analysed using ImageJ for unbiased quantification. Mean MT-CO1 intensity measured relative to CAIX expression and was compared between tumour tissues and tumour organoids. The MT-CO1-stained image of tumour tissue (middle left panel) represents the same image as shown in Fig. 2F (upper right panel). t: tissue, o: organoid, T: tumour, H: healthy tissue. Sample sizes are indicated within group labels. Statistical significance is indicated by asterisks, with the symbol of * indicating $p < 0.05$. (For interpretation of the references to colour in this figure legend, the reader is referred to the web version of this article.)

SDHA is most likely associated with SDHAF2. Moreover, the persistence of dysfunctional CII may point to secondary function of the CII_{low} subassembly, potentially aiding tumour progression/metastasis via distinct mechanisms that are not clear at present.

We have yet to determine the underlying cause of the simultaneous upregulation of mitochondrial function and imbalance in CII assembly in high-grade ccRCC tumours. Our investigation implicates CII_{low} as a potential negative prognostic marker in ccRCC, reflecting its role in promoting tumorigenesis and metastasis.

Models that recapitulate patient tumours are scarce and not highly reliable. A recent and potentially promising approach is the use of organoids derived from tumours. Here, we show successful preparation of organoids from tumour tissue of seven ccRCC patients, with these organoids preserving the histological architecture of the parental tissue. They presented as small, cell-dense, non-cystic structures without distinct organization and morphology, as shown previously [48].

To determine whether phenotypic features found in tumour tissue are retained in vitro, we characterized the organoids. The search for a reliable marker of RCC remains challenging. We found that CAIX is expressed in ccRCC tumours, but not in papillary and chromophobe RCC or renal oncocytoma, as shown previously [49]. This suggests that ccRCC tumours likely reflect a pseudo-hypoxic environment controlled by HIF1α signaling. CAIX plays a key role in adapting to hypoxia by regulating pH through converting carbon dioxide to bicarbonate and protons, enabling cancer cells to survive and thrive in low-oxygen conditions [50]. Our tumour organoids resemble the parental tumour tissue in that they are positive for CAIX, indicating preservation of this pseudo-hypoxic environment marker, as supported by the literature [51]. To test whether RCC organoids preserve the *VHL* variants of their parental tumours, amplicon sequencing was performed on seven established RCC organoids and their matching tumour samples. The shared known somatic variants in *VHL* found in the tumour tissues were conserved in all corresponding RCC organoids. These results confirm previous reports of preservation of *VHL* mutations in the majority of organoids derived from the respective primary tumours [52].

Regarding mitochondrial and CII properties, we found that organoids derived from tumours were similar to parental tumours in terms of decreased mitochondrial content and diminished CII properties. This is the first study to examine CII properties in RCC-derived organoids, highlighting their potential as a model of ccRCC. Additionally, these organoids could serve as valuable tools for mitochondrial research or pharmacological screening.

5. Conclusion

In summary, we demonstrate that decreased CII activity is a common feature in ccRCC, with adverse functional and prognostic implications. Additionally, elucidating the functional significance of altered CII assembly dynamics observed in high-grade tumours could provide valuable insights into tumour progression. While the precise mechanism(s) underlying this phenomenon remain elusive, our findings suggest a potential role for CII_{low} in driving tumorigenesis and metastasis. Overall, our findings contribute to deeper understanding of metabolic reprogramming in ccRCC and pave the way for future research aimed at identifying potential treatment strategies and improving patient outcomes, implying the use of tumour-derived organoids.

Supplementary data to this article can be found online at https://doi.org/10.1016/j.bbadis.2024.167556.

Funding

This work was supported in part by grants from Czech Health Foundation NU21-03-00545 to J.N., NU23-03-00226 to S.D., NU20-03-00309 to K.K., from Czech Science Foundation 23-05303S to S.Bo, and from MH CZ-DRO (Institute of Endocrinology – EÚ, 00023761) to J.V.

CRediT authorship contribution statement

Sona Miklovicova: Writing – review & editing, Writing – original draft, Visualization, Validation, Investigation, Formal analysis, Data curation, Conceptualization. **Luca Volpini:** Writing – review & editing, Writing – original draft, Methodology, Investigation, Conceptualization. **Ondrej Sanovec:** Validation, Methodology, Investigation. **Federica Monaco:** Investigation, Formal analysis, Data curation. **Katerina Hadrava Vanova:** Writing – review & editing, Writing – original draft, Resources, Methodology. **Jaromir Novak:** Visualization, Validation, Methodology, Investigation. **Stepana Boukalova:** Writing – review & editing, Writing – original draft, Supervision, Investigation, Conceptualization. **Renata Zobalova:** Methodology, Investigation, Data curation. **Petr Klezl:** Validation, Resources, Data curation. **Marco Tomasetti:** Supervision. **Vladimir Bobek:** Validation, Resources, Data curation. **Vojtech Fiala:** Validation, Resources, Data curation. **Josef Vcelak:** Software, Methodology, Investigation, Formal analysis, Data curation. **Lory Santarelli:** Validation, Supervision, Resources. **Zuzana Bielcikova:** Writing – review & editing, Writing – original draft, Resources, Investigation, Formal analysis, Conceptualization. **Katerina Komrskova:** Writing – review & editing, Writing – original draft, Supervision, Resources. **Katarina Kolostova:** Writing – review & editing, Writing – original draft, Validation, Resources, Data curation. **Karel Pacak:** Writing – review & editing, Writing – original draft, Supervision, Resources. **Sarka Dvorakova:** Writing – review & editing, Writing – original draft, Supervision, Project administration, Funding acquisition, Data curation, Conceptualization. **Jiri Neuzil:** Writing – review & editing, Writing – original draft, Supervision, Resources, Funding acquisition, Conceptualization.

Declaration of competing interest

We declare here that no co-author has any clash of interest.

Acknowledgements

We thank Prof Michael V. Berridge (Malaghan Institute for Medical Research, Wellington, New Zealand) for critical reading and editing this manuscript.

Data availability

Data will be made available on request.

References

[1] U. Capitanio, et al., Epidemiology of renal cell carcinoma, Eur. Urol. 75 (1) (2019) 74–84, https://doi.org/10.1016/j.eururo.2018.08.036.
[2] R.L. Siegel, K.D. Miller, A. Jemal, Cancer statistics, 2020, CA Cancer J. Clin. 70 (1) (2020) 7–30, https://doi.org/10.3322/caac.21590.
[3] D. Lindgren, et al., Cell-type-specific gene programs of the normal human nephron define kidney cancer subtypes, Cell Rep. 20 (6) (2017) 1476–1489, https://doi.org/10.1016/j.celrep.2017.07.043.
[4] Y. Sato, et al., Integrated molecular analysis of clear-cell renal cell carcinoma, Nat. Genet. 45 (8) (2013) 860–867, https://doi.org/10.1038/ng.2699.
[5] M. Ivan, et al., HIFα targeted for VHL-mediated destruction by proline hydroxylation: implications for O2 sensing, Science 292 (5516) (2001) 464–468, https://doi.org/10.1126/science.1059817.
[6] B.I. Rini, S.C. Campbell, B. Escudier, Renal cell carcinoma, Lancet 373 (2009) 1119–1151, https://doi.org/10.1016/S0140.
[7] S. Fuhrman, L. Lasky, C. Limas, Prognostic significance of morphologic parameters in renal cell carcinoma, Am. J. Surg. Pathol. 6 (7) (1982) 655–663.
[8] H. Moch, A.L. Cubilla, P.A. Humphrey, V.E. Reuter, T.M. Ulbright, The 2016 WHO classification of tumours of the urinary system and male genital organs—part a: renal, penile, and testicular tumours, Eur Urol 70 (1) (2016) 93–105, https://doi.org/10.1016/j.eururo.2016.02.029.
[9] R.K. Aggarwal, et al., Functional succinate dehydrogenase deficiency is a common adverse feature of clear cell renal cancer 118 (2021) 2106947118, https://doi.org/10.1073/pnas.2106947118/-/DCSupplemental.
[10] T.M. Iverson, P.K. Singh, G. Cecchini, An evolving view of complex II—noncanonical complexes, megacomplexes, respiration, signaling, and beyond, J. Biol. Chem. 299 (6) (2023), https://doi.org/10.1016/j.jbc.2023.104761.
[11] A. Bezawork-Geleta, J. Rohlena, L. Dong, K. Pacak, J. Neuzil, Mitochondrial Complex II: At the Crossroads, Trends Biochem. Sci. 42 (4) (2017), https://doi.org/10.1016/j.tibs.2017.01.003.
[12] P. Sharma, et al., Disordered-to-ordered transitions in assembly factors allow the complex II catalytic subunit to switch binding partners, Nat. Commun. 15 (1) (2024), https://doi.org/10.1038/s41467-023-44563-7.
[13] A. Bezawork-Geleta, et al., Alternative assembly of respiratory complex II connects energy stress to metabolic checkpoints, Nat. Commun. 9 (1) (2018), https://doi.org/10.1038/s41467-018-04603-z.
[14] K. Rohlenova, et al., Selective disruption of respiratory supercomplexes as a new strategy to suppress Her2high breast cancer, Antioxid. Redox Signal. 26 (2) (2017) 84–103, https://doi.org/10.1089/ars.2016.6677.
[15] Z. Bielcikova, et al., Mitochondrially targeted tamoxifen as anticancer therapy: case series of patients with renal cell carcinoma treated in a phase I/Ib clinical trial, Ther. Adv. Med. Oncol. 15 (2023), https://doi.org/10.1177/17588359231197957.
[16] Z. Bielcikova, et al., Mitochondrially targeted tamoxifen in patients with metastatic solid tumours: an open-label, phase I/Ib single-Centre trial, EClinicalMedicine 57 (2023), https://doi.org/10.1016/j.eclinm.2023.101873.
[17] N. Saxena, et al., SDHB-deficient cancers: the role of mutations that impair iron sulfur cluster delivery, J. Natl. Cancer Inst. 108 (1) (2016), https://doi.org/10.1093/jnci/djv287.
[18] K. Chung, et al., Structural and molecular interrogation of intact biological systems, Nature 497 (7449) (2013) 332–337, https://doi.org/10.1038/nature12107.
[19] J. Ding, et al., CT-based radiomic model predicts high grade of clear cell renal cell carcinoma, Eur. J. Radiol. 103 (2018) 51–56, https://doi.org/10.1016/j.ejrad.2018.04.013.
[20] J. Shu, et al., Clear cell renal cell carcinoma: CT-based radiomics features for the prediction of Fuhrman grade, Eur. J. Radiol. 109 (2018) 8–12, https://doi.org/10.1016/j.ejrad.2018.10.005.
[21] A. Becker, et al., Critical analysis of a simplified Fuhrman grading scheme for prediction of cancer specific mortality in patients with clear cell renal cell carcinoma - impact on prognosis, Eur. J. Surg. Oncol. 42 (3) (2016) 419–425, https://doi.org/10.1016/j.ejso.2015.09.023.
[22] M.L. Hart, et al., Mitochondrial redox adaptations enable alternative aspartate synthesis in SDH-deficient cells, Elife 12 (2023), https://doi.org/10.7554/elife.78654.
[23] K. Čunátová, et al., Mitochondrial translation is the primary determinant of secondary mitochondrial complex I deficiencies, iScience (2024) 110560, https://doi.org/10.1016/j.isci.2024.110560.
[24] M.L. Nickerson, et al., Improved identification of von Hippel-Lindau gene alterations in clear cell renal tumors, Clin. Cancer Res. 14 (15) (2008) 4726–4734, https://doi.org/10.1158/1078-0432.CCR-07-4921.
[25] A.C. Young, et al., Analysis of VHL gene alterations and their relationship to clinical parameters in sporadic conventional renal cell carcinoma, Clin. Cancer Res. 15 (24) (2009) 7582–7592, https://doi.org/10.1158/1078-0432.CCR-09-2131.
[26] A.A. Batavia, P. Schraml, H. Moch, Clear cell renal cell carcinoma with wild-type von Hippel-Lindau gene: a non-existent or new tumour entity? Histopathology 74 (1) (2019) https://doi.org/10.1111/his.13749.
[27] J. Hu, et al., Tumor heterogeneity in VHL drives metastasis in clear cell renal cell carcinoma, Signal Transduct. Target. Ther. 8 (1) (2023), https://doi.org/10.1038/s41392-023-01362-2.
[28] P. Hudler and M. Urbancic, The Role of VHL in the Development of von Hippel-Lindau Disease and Erythrocytosis, Genes (Basel), vol. 13, no. 2, doi:https://doi.org/10.3390/genes13020362.
[29] A. Serghini, et al., Characterizing and predicting ccRCC-causing missense mutations in Von Hippel-Lindau disease, Hum. Mol. Genet. 33 (3) (2024) 224–232, https://doi.org/10.1093/hmg/ddad181.
[30] Y. Xiao, et al., Decreased mitochondrial DNA content drives OXPHOS dysregulation in chromophobe renal cell carcinoma, Cancer Res. 80 (18) (2020) 3830–3840, https://doi.org/10.1158/0008-5472.CAN-20-0754.
[31] E.L. LaGory, et al., Suppression of PGC-1α is critical for reprogramming oxidative metabolism in renal cell carcinoma, Cell Rep. 12 (1) (2015) 116–127, https://doi.org/10.1016/j.celrep.2015.06.006.
[32] S. Li, et al., Impaired oxygen-sensitive regulation of mitochondrial biogenesis within the von Hippel–Lindau syndrome, Nat. Metab. 4 (6) (2022) 739–758, https://doi.org/10.1038/s42255-022-00593-x.
[33] H. Zhu, X. Wang, S. Lu, K. Ou, Metabolic reprogramming of clear cell renal cell carcinoma, Frontiers Media S.A. (2023), https://doi.org/10.3389/fendo.2023.1195500.
[34] Z. Liu, et al., Mitochondrial NDUFA4L2 is a novel regulator of skeletal muscle mass and force, FASEB J. 35 (12) (2021), https://doi.org/10.1096/fj.202100066R.
[35] J.M. Kubala, et al., NDUFA4L2 reduces mitochondrial respiration resulting in defective lysosomal trafficking in clear cell renal cell carcinoma, Cancer Biol. Ther. 24 (1) (2023), https://doi.org/10.1080/15384047.2023.2170669.
[36] D. Bezwada, et al., Mitochondrial complex I promotes kidney cancer metastasis, Nature (2024), https://doi.org/10.1038/s41586-024-07812-3.
[37] J. Tian, et al., Targeting oxidative phosphorylation to increase the efficacy of immune-combination therapy in renal cell carcinoma, J. Immunother. Cancer 12 (2) (2024) e008226, https://doi.org/10.1136/jitc-2023-008226.
[38] D. Meierhofer, et al., Decrease of mitochondrial DNA content and energy metabolism in renal cell carcinoma, Carcinogenesis 25 (6) (2004) 1005–1010, https://doi.org/10.1093/carcin/bgh104.
[39] F. Martínez-Jiménez, et al., Pan-cancer whole-genome comparison of primary and metastatic solid tumours, Nature 618 (7964) (2023) 333–341, https://doi.org/10.1038/s41586-023-06054-z.
[40] K. Takeda, S. Bastacky, R. Dhir, M. Mohebnasab, G.M. Quiroga-Garza, Morphological characteristics of SETD2-mutated locally advanced clear cell renal cell carcinoma: comparison with BAP1-mutated clear cell renal cell carcinoma, Ann. Diagn. Pathol. 68 (2024), https://doi.org/10.1016/j.anndiagpath.2023.152223.
[41] J. Liu, et al., Loss of SETD2 induces a metabolic switch in renal cell carcinoma cell lines toward enhanced oxidative phosphorylation, J. Proteome Res. 18 (1) (2019) 331–340, https://doi.org/10.1021/acs.jproteome.8b00628.
[42] N.J. Coffey, M.C. Simon, Metabolic alterations in hereditary and sporadic renal cell carcinoma, Nature Research (2024), https://doi.org/10.1038/s41581-023-00800-2.
[43] K.M. Cornejo, et al., Succinate dehydrogenase B: a new prognostic biomarker in clear cell renal cell carcinoma, Hum. Pathol. 46 (6) (2015) 820–826, https://doi.org/10.1016/j.humpath.2015.02.013.
[44] J.B. Neves, et al., Defining the origin, evolution, and immune composition of SDH-deficient renal cell carcinoma, iScience 25 (11) (2022), https://doi.org/10.1016/j.isci.2022.105389.
[45] C.J. Ricketts, et al., Kidney tumors associated with germline mutations of FH and SDHB show a CpG island methylator phenotype (CIMP), PloS One 17 (12 December) (2022), https://doi.org/10.1371/journal.pone.0278108.
[46] Z. Fang, Q. Sun, H. Yang, J. Zheng, SDHB suppresses the tumorigenesis and development of ccRCC by inhibiting glycolysis, Front. Oncol. 11 (2021), https://doi.org/10.3389/fonc.2021.639408.
[47] J. Yang, et al., Functional deficiency of succinate dehydrogenase promotes tumorigenesis and development of clear cell renal cell carcinoma through weakening of ferroptosis, Bioengineered 13 (4) (2022) 11187–11207, https://doi.org/10.1080/21655979.2022.2062537.
[48] C. Calandrini, et al., An organoid biobank for childhood kidney cancers that captures disease and tissue heterogeneity, Nat. Commun. 11 (1) (Dec. 2020), https://doi.org/10.1038/s41467-020-15155-6.
[49] A. Luong-Player, H. Liu, H.L. Wang, F. Lin, Immunohistochemical reevaluation of carbonic anhydrase IX (CA IX) expression in tumors and normal tissues, Am. J. Clin. Pathol. 141 (2) (2014) 219–225, https://doi.org/10.1309/AJCPVJDS28KNYZLD.
[50] H.M. Becker, Carbonic Anhydrase IX and Acid Transport in Cancer, Springer Nature, 2020, https://doi.org/10.1038/s41416-019-0642-z.
[51] Y. Xue, et al., Patient-derived organoids potentiate precision medicine in advanced clear cell renal cell carcinoma, Precis. Clin. Med. 5 (4) (2022), https://doi.org/10.1093/pcmedi/pbac028.
[52] Z. Li, et al., Patient-derived renal cell carcinoma organoids for personalized cancer therapy, Clin. Transl. Med. 12 (7) (2022), https://doi.org/10.1002/ctm2.970.
[53] C. Kukat, et al., Cross-strand binding of TFAM to a single mtDNA molecule forms the mitochondrial nucleoid, Proc Natl Acad Sci U S A 12 (36) (2015) 11288–11293, https://doi.org/10.1073/pnas.1512131112.